



# Response and prediction of unsaturated permeability of loess to microstructure

Haiman Wang · Wankui Ni

Received: 18 July 2022 / Accepted: 5 January 2023  
© The Author(s) 2023

**Abstract** The study of water infiltration helps to investigate the pollutants' migration, grasp the mechanism of the water cycle, and correctly evaluate water resources. This paper reveals the mechanism of compacted loess's one-dimensional vertical water infiltration characteristics using a low-cost water infiltration device. In addition, it investigates particle arrangement and pore size distribution characteristics using nuclear magnetic resonance (NMR) and scanning electron microscopy (SEM). The test finding suggests that the loess's early-stage infiltration rate is significant, and the dry density is not related to the infiltration characteristics. With the advance of the wetting front, the infiltration rate decreases under air resistance. The unsaturated permeability decreases with dry density at lower matric suction while unaffected by the dry density at higher matric suction. Moreover, the volume and connectivity of pores mainly control the water infiltration characteristics. Finally, based on the test results, a method for rapidly predicting the unsaturated permeability of loess is proposed. The results of the study help predict contaminant transport and guide groundwater extraction and management.

## Highlights

1. Loess's unsaturated infiltration characteristics with different dry densities were obtained.
2. The relationship between loess's unsaturated permeability and microstructure was investigated.
3. An unsaturated permeability prediction model based on basic physical indices is proposed.

**Keywords** Loess · Permeability · Microstructure · Pore size distribution curve · Wetting front

## 1 Introduction

The hydrological cycle depends heavily on soil, especially topsoil, which is a critical part of the natural ecosystem. Rainfall infiltration, surface evaporation, and dynamic soil water storage are all accomplished in a soil medium. Loess is a regional soil deposited under arid and semi-arid conditions and covers an area of about 324,600 km<sup>2</sup> in northwest China (Peng et al. 2019). As the primary construction material in the loess area, loess is prone to collapse and other hazards during water infiltration (Wang et al. 2021a, 2021c). Water infiltration is also one of the main factors for frequent slope damage and landslides in loess areas with seasonal rainfall (Au 1993; Chen et al. 2004; Kassim et al. 2012; Galeandro et al. 2014; Jones and Rowe 2016). In a human social environment where various pollutants are present in large

---

H. Wang · W. Ni (✉)  
College of Geological Engineering and Geomatics,  
Chang'an University, Xi'an 710054, Shaanxi,  
People's Republic of China  
e-mail: 18700425209@163.com; niwankui@chd.edu.cn

H. Wang  
e-mail: 2020026006@chd.edu.cn

quantities, the downward transport of pollutants with water can contaminate soil and groundwater. The pore space in loess is a natural channel for water transport. Therefore, investigating water infiltration in loess is essential in preventing and controlling geological hazards and optimizing the human environment.

Soil permeability is an essential characteristic of geotechnical engineering (Liu et al. 2016; Gao et al. 2018; Xu et al. 2020), which influences the engineering behavior (Ma et al. 2017; Wang et al. 2018) and the capacity to transport pollutants (Gao et al. 2018; Li et al. 2018). Multiple researchers have extensively investigated the saturated permeability of various soil types worldwide (Bevington et al. 2016; Damiano et al. 2017; Zhang et al. 2019b; Hou et al. 2020; Wang et al. 2020; Xu et al. 2020). However, due to several limitations of unsaturated permeability measurements, they have not been classified as design parameters so far (Shackelford et al. 2000; Aldaeef and Rayhani 2014). Although unsaturated permeability has not been adequately studied, researchers have recognized dry density as a critical factor affecting loess permeability (Cai et al. 2014; Jing et al. 2022). Furthermore, the mechanism of unsaturated permeability variation in compacted loess is unclear. Soil microstructure is the primary determinant of macroscopic properties (Shao et al. 2018; Li et al. 2019b; Wang et al. 2019). The unsaturated permeability is closely related to the microstructure of the loess. Since it is difficult to accurately describe the structural changes within the soil by conducting macroscopic tests, investigating loess's unsaturated permeability using soil microstructure has become an essential technique. Consequently, a number of tests on permeability and microstructure is required to investigate the response of permeability to microstructure.

In the past decades, many theories have been developed to predict soil's unsaturated permeability due to the difficulty in measuring this parameter (Gao et al. 2021). For instance, influenced by the pore size distribution, Mualem (1976) and Fredlund et al. (1994) proposed estimating unsaturated permeability using soil and water retention curves. In the twenty-first century, researchers began to use conventional soil data to assess unsaturated permeability (Wagner et al. 2001; Zhuang et al. 2001). Zand-Parsa and Sepaskhah (2004) proposed an unsaturated permeability equation based on the area of the liquid–gas interface around the particles. The prediction model proposed by Lebeau and

Konrad (2010) takes the capillary and thin film flow into account. Gao and Shao (2015) considered the effect of temperature. Despite the extensive research on unsaturated permeability prediction, unsaturated permeability prediction models considering dry density/porosity ratio are still poorly described. Therefore, further research is needed on unsaturated relative permeability prediction methods that consider the effects of porosity and dry density.

This study uses a low-cost one-dimensional soil column percolation device to conduct permeability tests, and SEM and NMR are adopted to observe its microstructure. The major objectives of this study are as follows: (1) Evaluate the infiltration characteristics; (2) Measure the microstructure of different dry density specimens to reveal the mechanism of water infiltration in loess; (3) Propose a microstructure-based model that describes unsaturated permeability with different void ratios; (4) Compare the measured data against the predicted values using the proposed permeability model.

## 2 Study areas

The study area is situated in Longde County, Guyuan City. The stratigraphic distribution of the area is characterized by Maran loess overlying clay. One landslide developed in this region is about 220 m in length and 249 m in width (Fig. 1). Typically, the sliding belt in the area forms at the contact surface between loess and mudstone. The hydraulic conductivity of loess is significantly greater than clay, so during rainfall, water enters the slope through the loess and collects at the contact surface of the clay and loess. The action of water rapidly softens the loess and clay, thereby reducing the stability of the landslide. Therefore, it is practical to investigate the infiltration characteristics of loess in this region for landslide management.

## 3 Materials and methods

### 3.1 Materials

The material used in this study was Malan loess obtained from the above-mentioned landslide. Table 1 lists the fundamental physical indicators of loess. The tested loess consists primarily of silt ( $2 \leq d \leq 75 \mu\text{m}$ )

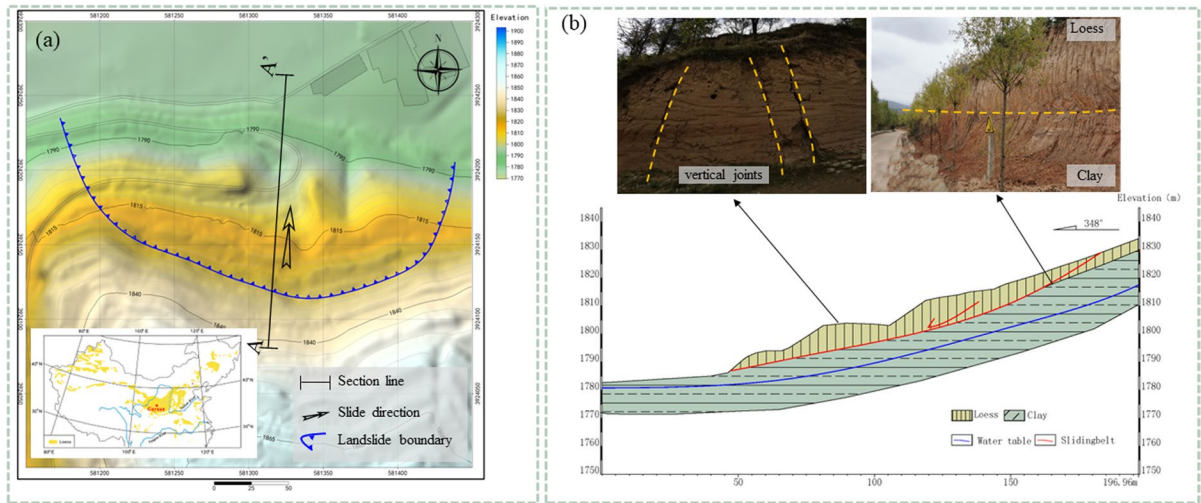


**Fig. 1** The Wenbu landslide: **a** location of the landslide; **b** geological section A–A’

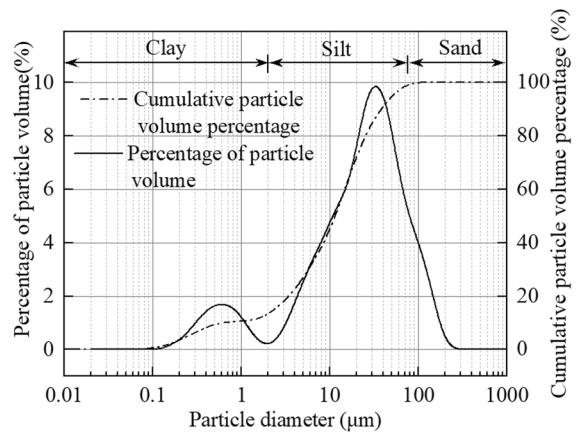
**Table 1** Major physical properties of loess

Property	Value
Maximum dry density $\rho_d$ (g/cm <sup>3</sup> )	1.69
Optimal water content $w_o$ (%)	14.11
Specific gravity $G_s$	2.72
Liquid limit $w_L$ (%)	28.9
Plastic limit $w_p$ (%)	16.1

grains (about 78.99%), with approximately the same sand ( $d > 75 \mu\text{m}$ ) and clay ( $d < 2 \mu\text{m}$ ) content of 10.39% and 10.62%, respectively (Fig. 2).

### 3.2 Experimental apparatus

The unsaturated permeability test instrument was a low-cost one-dimensional infiltration test device (Fig. 3). It consists of a Plexiglas barrel, a steel base, and a counterforce frame. The plexiglass barrel measures 63 cm in height, 30 cm in diameter, and 1 cm in wall thickness. The Plexiglas barrel is evenly distributed with small holes on both sides which have a diameter of 0.8 cm and a vertical spacing of 10 cm. The MPS-6 and EC-5 sensors were buried in small holes for matric suction ( $\psi$ ) and volumetric water content ( $\theta$ ) testing at each height. Four threaded tie rods hold the Plexiglas barrel securely to the steel base. Permeable holes with a 5 mm diameter are uniformly distributed at the base of the soil column. A

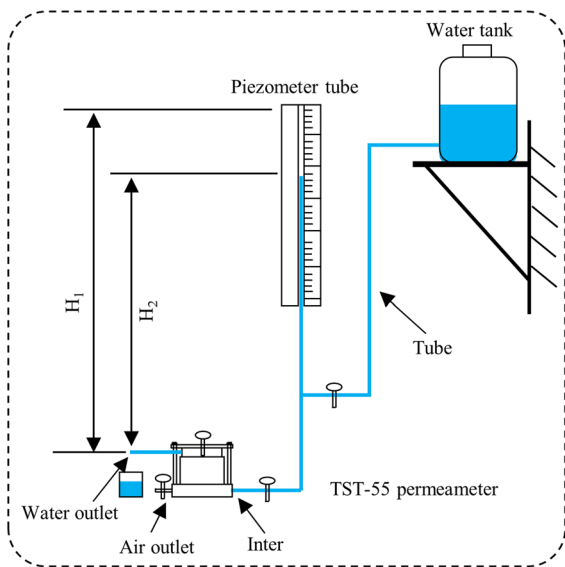
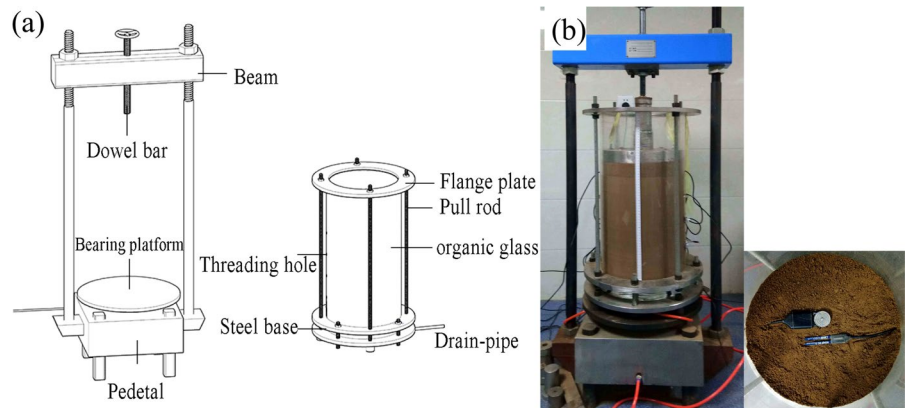


**Fig. 2** Particle size distribution (PSD) of test loess

drainage pipe discharges water from beneath the permeable hole.

### 3.3 Methods

The loess retrieved from the site was broken with a rubber hammer and air-dried. Pass the air-dried loess through a 2 mm sieve. Optimal water content is achieved by spraying water evenly into the soil. The soil is sealed and maintained for 72 h to ensure uniform water distribution within it.

**Fig. 3** Vertical infiltration device**Fig. 4** Saturated permeation test device

### 3.3.1 Saturated permeability test

A metal mold is employed for statically compacted soil. The  $\rho_d$  of the specimens were 1.45, 1.55, and 1.65 g/cm<sup>3</sup>, respectively. The dry density of the specimens used for saturation infiltration and the soil columns utilized for subsequent one-dimensional infiltration tests were kept consistent. Therefore, the results of the saturation permeability test can be used to determine the saturation permeability of the soil column. The variable head method measured the saturation permeability at  $20 \pm 2$  °C. Nanjing Soil

Instrument Factory produced the instrument used in this study (Fig. 4). The specific operation steps were reported in Yuan et al. (2022). The variable head permeability was determined using the following formula:

$$k_s = 2.3 \frac{aL}{A(t_2 - t_1)} \log \frac{H_1}{H_2} \quad (1)$$

where  $k_s$  is the permeability (cm/s),  $A$  is the cross-sectional area of the sample (cm<sup>2</sup>),  $a$  is the cross-sectional area of the tube (cm<sup>2</sup>),  $L$  is the height of the sample (cm), and  $t_1$  and  $t_2$  are the start and end times of the test (s), respectively.

### 3.3.2 One-dimensional soil column permeability test

In Plexiglas drums, the soil was compacted in layers to densities of 1.45, 1.55, and 1.65 g/cm<sup>3</sup> following maintenance. The specific steps are outlined below. The soil mass necessary for a 5-cm high column is calculated from the soil's  $\rho_d$  and water content ( $w$ ). The soil is evenly spread on the bottom of the Plexiglas barrel and compacted to the desired height using the self-contained pressurizing device. The above steps were repeated ten times, with each layer 5 cm reaching a height of 5 cm. The sensors were spaced 10 cm apart in four groups. Soil columns were constructed and then dried naturally to monitor changes in  $\theta$  and  $\psi$  throughout the process from drying to saturation. The infiltration test is conducted after the sensor reading has stabilized. Observe the water infiltration process during the test and record it in time.

When water flows out of the drainage pipe, measure the water flow rate regularly.

The soil mass required for a 5 cm high soil column is calculated using the following formula:

$$m_s = A_p \cdot h_5 \cdot \rho_d(1 + w_o) \tag{2}$$

where  $m_s$  is the soil mass required for a 5 cm high soil column (g),  $A_p$  is the bottom area of the plexiglass drum (cm<sup>2</sup>), and  $h_5$  is the height of the soil column, which is 5 cm in this case.

The total head  $h_w$  is the sum of the positional head  $h$  and the matric suction head  $h_m$ , i.e.:

$$h_w = h + h_m \tag{3}$$

The hydraulic gradient  $i_w$  is the slope of the total head distribution along the soil column, i.e.:

$$i_w = \frac{dh_w}{dh} \tag{4}$$

The volume of water between the  $h$  point and the bottom of the soil column is:

$$V_w = \int_0^h \theta_w(h)_t Adh \tag{5}$$

where  $\theta_w(h)_t$  is the volumetric water content at point  $h$  at time  $t$ .

The flow velocity  $v_w$  at point  $h$  can be defined as:

$$v_w = \frac{dV_w}{Adt} \tag{6}$$

The unsaturated permeability is:

$$k_w = -\frac{v_w}{i_{ave}} \tag{7}$$

where  $i_{ave}$  is the average hydraulic gradient.

The forward differential method is applied to calculate  $i_{ave}$ :

$$i_{ave} = \frac{1}{2} \left( \frac{h_w(h2),t1 - h_w(h1),t1}{h2 - h1} + \frac{h_w(h2),t2 - h_w(h1),t2}{h2 - h1} \right) \tag{8}$$

where  $h_w(h),t$  is the water head at point  $h$  at time  $t$  (cm).

Based on the  $\psi$  and  $\theta$ , the instantaneous profile method described above can compute the unsaturated permeability  $s$  of compacted loess at various dry densities.

### 3.3.3 NMR test

After the one-dimensional soil column infiltration test, the samples were cutting with a cutting ring inside the soil column. The PQ-001 mini NMR instrument developed by Suzhou Newman was used for NMR testing. Nuclear magnetic resonance is a technique for testing hydrogen protons. Notably, the ferromagnetic material in traditional stainless steel ring cutters can affect the homogeneity of the main magnetic field in the NMR analyzer. In this experiment, a PTFE ring cutter replaced the traditional stainless steel ring cutter. When pores are saturated with water, the hydrogen proton distribution corresponds to the pore size distribution (PSD). Due to the difficulty of achieving full soil saturation at standard atmospheric pressure, the specimen should be vacuum-saturated before the NMR test to evaluate the entire PSD curve. The specific operational steps have been reported by Wang et al. (2021a). Transverse relaxation time ( $T_2$ ) curves are used to depict the test results. The  $T_2$  curves can be converted into pore size distribution curves (Kong et al. 2017; Wang et al. 2021a, 2021b).

### 3.3.4 SEM test

The surface soil of the intact block sample was carefully and uniformly removed to prevent disturbing the soil sample structure during NMR testing. Then, a cubic stick with dimensions of 10×10×20 mm (L×W×H) was trimmed from the core of the intact block sample. The conventional air-drying method causes soil samples to shrink and deform. In this study, the sticks were dehydrated in a freeze dryer to eliminate the potential influence of water on the subsequent microstructure observations (Wei et al. 2020). Then, create a minor groove in the middle of the soil column. A flat fresh surface was obtained by breaking the groove before the test. A representative section was selected for observation. The MLA650F SEM developed by FEL was used for SEM imaging.

The microstructure of compacted loess was investigated using NMR and SEM techniques. Figure 5 displays the testing procedure is shown in.

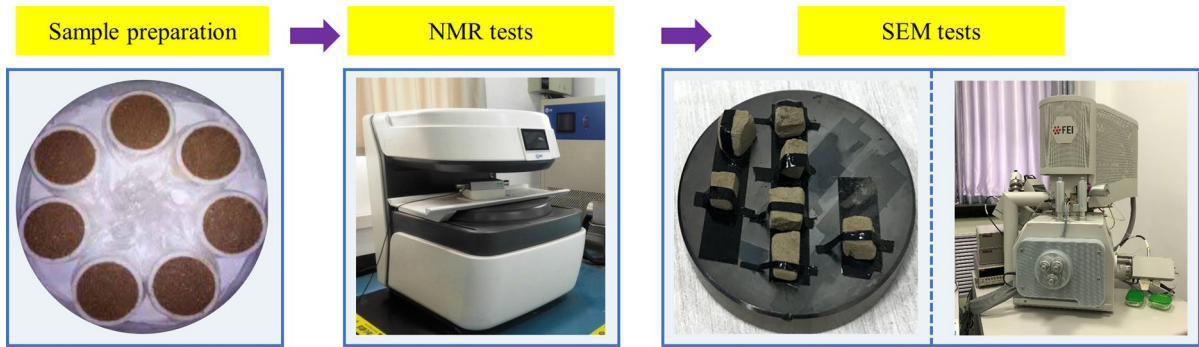


Fig. 5 Flowchart of microstructure testing

### 4 Results

#### 4.1 One-dimensional infiltration characteristics

##### 4.1.1 Time series curves of cumulative infiltration volume and infiltration rate

Since the cross-sectional area of the soil column is constant, the infiltration volume is given as the volume of water infiltrated per unit area  $Q$  (Fig. 6). The cumulative infiltration volume gradually increases with the increase in infiltration duration. However, the infiltration rate shows an opposite trend, decreasing with the increase in time and stabilizing at a fixed value. On the other hand, the cumulative infiltration and the infiltration rate are negatively correlated with the dry density.

The cumulative infiltration and infiltration rate time series curve can be divided based on the shape

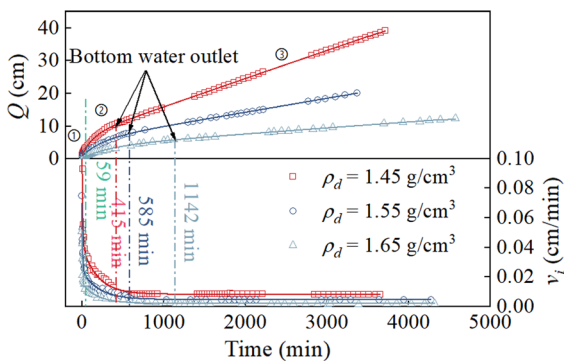


Fig. 6 Cumulative infiltration volume ( $Q$ ) and infiltration rate ( $v_i$ ) time series curves

of the curve into a fast infiltration stage, a slow infiltration stage, and a stable infiltration stage. In the fast infiltration stage (0–59 min), the cumulative infiltration volume increases rapidly, indicating that the soil has a strong infiltration capacity. The infiltration rates of different dry densities overlap and show a rapidly decreasing trend. In the fast infiltration stage, the influence of dry densities is insignificant on the infiltration rate. The cumulative infiltration continues to increase during the slow infiltration stage until water emerges from the soil column. The time taken for water to emerge from the bottom of each dry-density soil column is 415, 585, and 1142 min, respectively. The time required for the saturation of the specimen gradually increases with the increase of the  $\rho_d$ . The infiltration rate decreases slowly in the slow infiltration stage, with the range of decreasing infiltration rate increasing with the rise in dry density. Therefore, at this stage, the time series curves start to diverge, and the cumulative infiltration for the same time reduces with the increase in  $\rho_d$ . In the stable infiltration stage, water is discharged from the soil column, which indicates that the column is close to saturation. Therefore, the cumulative infiltration of soil columns with different dry densities increases linearly with time, and the infiltration rates are stable at  $8.46 \times 10^{-3}$ ,  $4.42 \times 10^{-3}$ , and  $1.07 \times 10^{-3}$  cm/min, respectively.

##### 4.1.2 Wet front advance distance and rate time series curve

The wet and dry interfaces in the one-dimensional soil column are wetting fronts. The migration characteristics of the wetting fronts visually reflect the rapidity

of water infiltration in the soil. The transparent Plexiglas barrel provides the conditions for observing the migration characteristics of the wetting front with the naked eye. The wetting front kept moving forward as the soil column infiltration test proceeded (Fig. 7). The time series curve of the wetting front advancing distance ( $S$ ) is steeper in the initial stage, and the slope gradually decreases as the test proceeds. The time series curve of the wetting front advance rate ( $v_w$ ) shows that the advance rate is significant and decreases rapidly in the initial stage. In this stage, the soil is drier, has a strong infiltration capacity, and the wetting front migrates downward quickly. As infiltration proceeds, the upper layer of the soil gradually becomes saturated, and its infiltration capacity

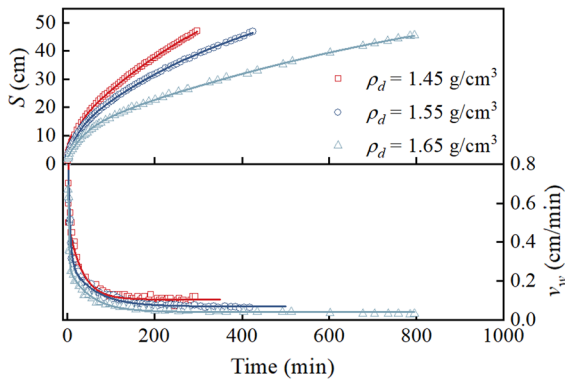


**Fig. 7** Time series curves of the wetting front advancing distance ( $S$ ) and rate ( $v_w$ )

gradually decreases. Thus, the wetting front migration rate decrease. The dry density also influences the wetting front advancing distance and rate. The wetting front advancing distance decreases with the increase in the  $\rho_d$ . It also influences the wetting front steady advance rate at the late infiltration stage. The wetting front steady advance rates for 1.45, 1.55, and 1.65 g/cm<sup>3</sup> dry density soil columns are 0.103, 0.067, and 0.034 cm/min, respectively.

4.1.3 Time series curves of  $\theta$  and  $\psi$  at monitoring points

The changes in  $\theta$  and  $\psi$  within the soil column during infiltration can be monitored with the help of sensors (Fig. 8). The changes in  $\theta$  and  $\psi$  at each position of the soil column can be divided into (i) a stable stage, (ii) a rapid change stage, and (iii) a slow change stage.

Before the water infiltration to the monitoring point, the time series curve is at stage (i), and the  $\theta$  and  $\psi$  are stable as the test proceeds sensors respond sequentially from shallow to deep. The time series curve enters stage (ii). Due to the different sensor response times, the time series curves diverge at stage (ii) (Table 2). The sensor’s response time at the same position increases with the increase in  $\rho_d$ . The sensor response time difference between soil columns with various  $\rho_d$  increases with the burial depth. For example, the sensor response time difference between the  $\rho_d$  of 1.45 g/cm<sup>3</sup> and 1.65 g/cm<sup>3</sup> soil columns is 16 min at 10 cm and 407 min at 40 cm. Both the

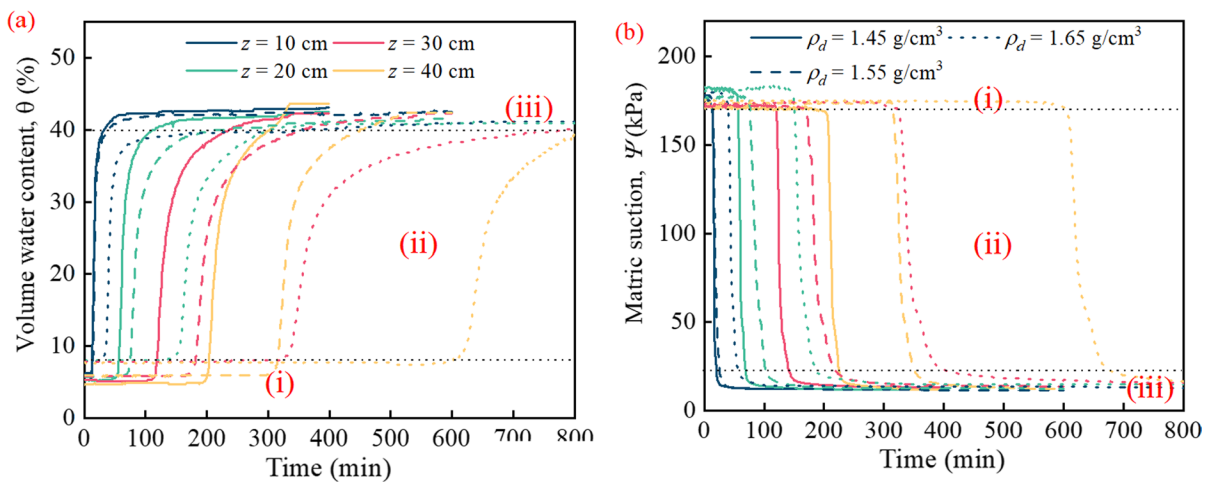


**Fig. 8** Time series curves of  $\theta$  and  $\psi$

**Table 2** Time required for sensor response at different burial depths

Dry density (g/ cm <sup>3</sup> )	Time (min)			
	10 cm	20 cm	30 cm	40 cm
1.45	10	46	103	196
1.55	12	60	166	299
1.65	26	137	322	603

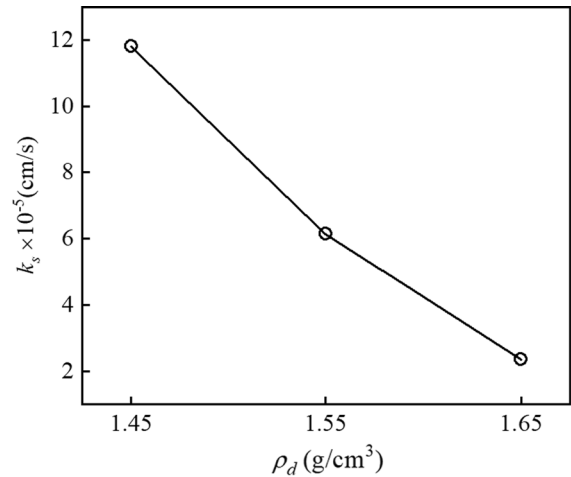
sensor response time and the response time difference between two adjacent sensors increase with the burial depth. For example, the response time difference between the sensors at 10 cm and 20 cm in a dry density of 1.45 g/cm<sup>3</sup> soil column is 36 min, and at 30 cm and 40 cm is 93 min. It indicates that the advancing speed of the wetting front gradually decreases, which is consistent with the results in Fig. 5. Moreover, the shape of the time series curve in stage (ii) corroborates the above results. Stage (ii) can be divided into a steep stage and a gentle stage. The steepening stage gradually decreases with the increase in  $\rho_d$  and burial depth. The time taken from the beginning of the sensor response to the end of the stage (ii) is defined as the humidification duration, which reflects the humidification rate of the soil (Table 3). The humidification duration increases gradually with the rise in dry density. In stage (iii), the volumetric water content and matric suction slowly change until each position's water content and matric suction are equal.

#### 4.1.4 Permeability

The results of the saturation permeability test are shown in Fig. 9. As shown in the figure, the saturation permeability of the three specimens is between  $10^{-5}$  and  $10^{-3}$  cm/min. As the dry density increases, the saturation permeability gradually decreases.

**Table 3** The humidification duration of loess at different monitoring points

Dry density (g/ cm <sup>3</sup> )	Time (min)			
	10 cm	20 cm	30 cm	40 cm
1.45	34	63	139	229
1.55	49	93	214	267
1.65	54	147	253	375

**Fig. 9** Saturated permeability  $k_s$ 

The unsaturated permeability of the loess can be calculated from Eqs. (2) to (8) and the data in Fig. 8 and the results are as shown in Fig. 10. This test is a humidification process, with a gradual increase in volumetric water content and a gradual decrease in  $\psi$ . The unsaturated permeability increases rapidly. The permeability is mainly distributed from  $10^{-9}$  to  $10^{-4}$  cm/min, spanning five orders of magnitude. The unsaturated permeability of different dry densities in the high suction section ( $\psi \geq 50$  kPa,  $\theta < 0.2$ ) overlap. The dry density has almost no effect on the permeability of loess when the  $w$  is low. As the matric suction decreases, the unsaturated permeability begins to diverge, with the smaller the  $\rho_d$ , the greater the permeability of the specimen. As the  $\psi$  decreases, the unsaturated permeability enters the saturation stage. As the  $\psi$  decreases, the saturation stage's permeability is almost constant. The air entry value ( $\psi_a$ ) is the turning point between the saturated and humidified stages (Fig. 10a). The dry density has a significant effect on the  $\psi_a$ , which increases as the  $\rho_d$  rises.

## 4.2 Microstructure

### 4.2.1 SEM results

The microstructure of loess specimens is observed in Fig. 11, with the particles, aggregates, and pores being visible. Generally, loess structure depends on the irregularity and randomness of the clay position. Most of the particles are encapsulated by clay to form



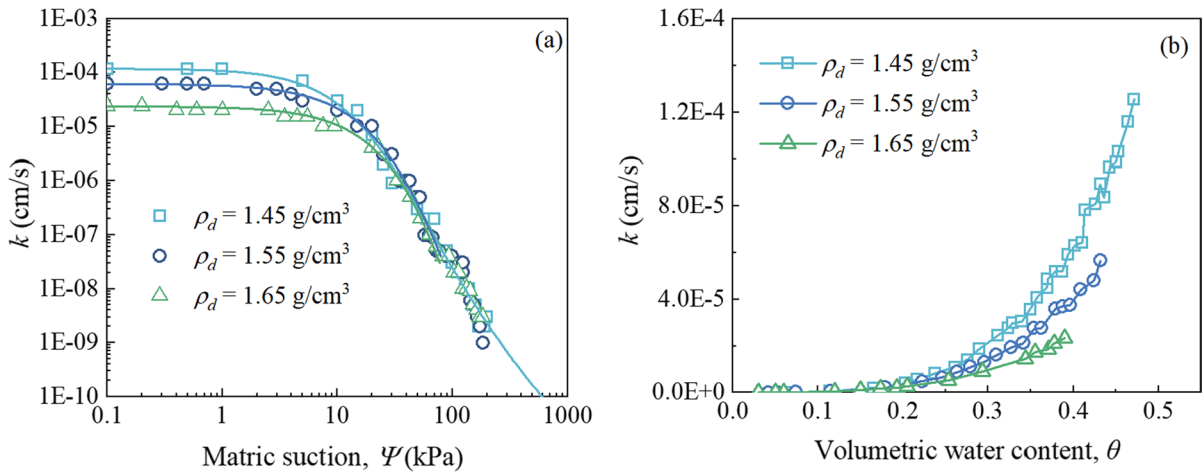


**Fig. 10** Unsaturated permeability  $k$  of specimens with various dry densities **a** expressed as matric suction; **b** expressed as volumetric water content

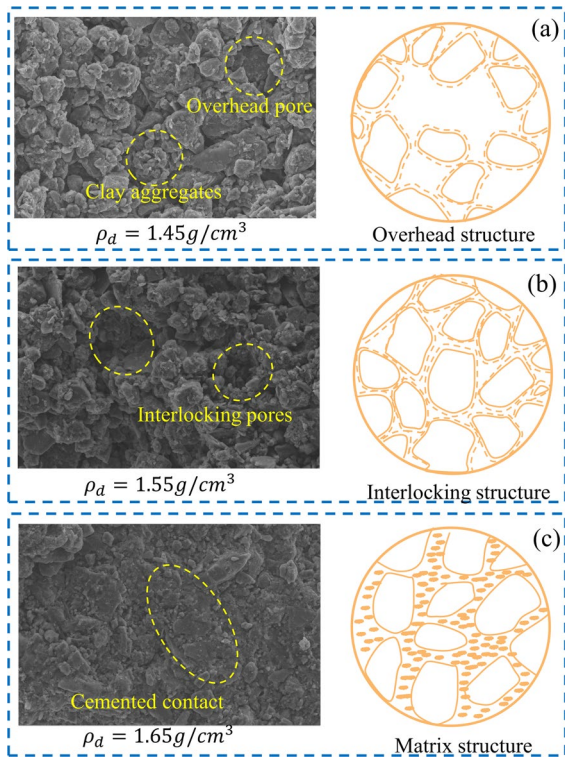


**Fig. 11** Microstructure of loess with different dry density

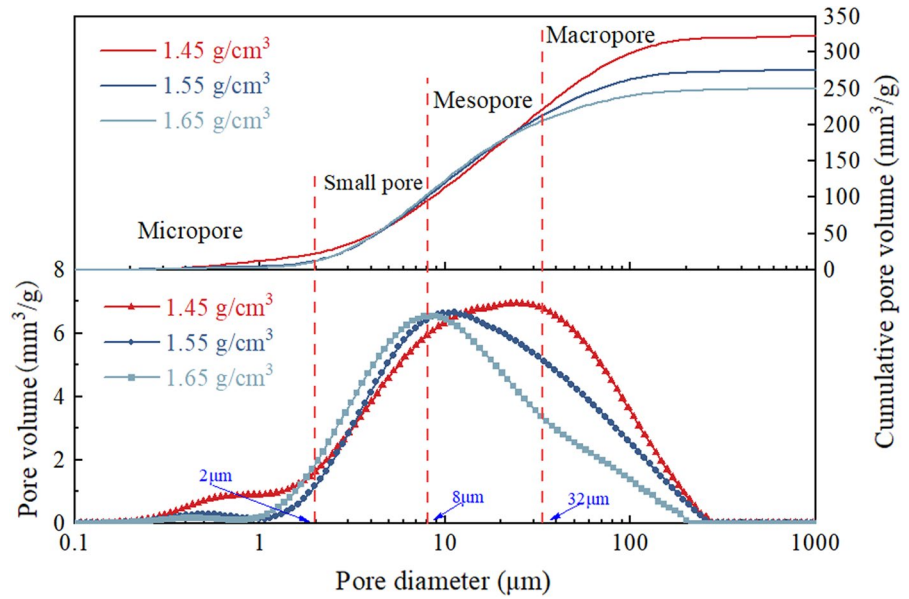
outer clay particles (Xie et al. 2018). Aggregates of varying sizes are formed between the outer clay particles through cementation. Moreover, large-diameter

aggregates form overhead structures (Fig. 11a). The larger the aggregates' diameter, the lower the stiffness and strength (Xu et al. 2021). The increase in dry density is essentially a process of soil compaction in which aggregates break up into smaller ones. The pores are filled with aggregate particles, resulting in a reduction of the total pore area and a deterioration of the pore connectivity (Fig. 11b). Thus, the fragmentation degree of aggregates in a cemented state is proportional to the dry density (Fig. 11c). In terms of particle skeleton, as the dry density increases, the broken aggregates fill the pores in the form of interlocking (Fig. 11b). The aggregates do not break continuously. When the dry density reaches a certain level, the aggregates can only reduce the void ratio by cementing with the skeletal particles. The cementation of the aggregate and skeleton particles blends the skeleton particle profile to form a matrix structure (Fig. 11c). In general, the particles' contact relationship increases with the dry density from an overhead structure to an interlocking structure to a matrix structure.

4.2.2 NMR results

The particle and aggregate arrangement and combination forms of various dry densities were analyzed using SEM images, and then the pore size distribution properties were analyzed using NMR results (Fig. 12). The specimens' pore size distribution

**Fig. 12** Pore size distribution curve



curves mainly exhibit a single-peak distribution and conform to a normal distribution in semi-logarithmic coordinates (Li et al. 2020b). As the dry density increases, pore diameters that exceed 10 μm are significantly compressed, and the maximum pore diameter decreases. There is a slight compression of the pore volume for pore sizes below 2 μm. The overall pore size distribution curve shrinks towards the middle, i.e., a smaller pore size distribution range. Compression makes the pore space more uniformly distributed in the soil. The pore diameter corresponding to the peak point of the PSD curve is the advantage pore diameter ( $d_a$ ), and the  $d_a$  decreases with the increase in dry density. For example, when the  $\rho_d$  of the specimen is increased from 1.45 g/cm<sup>3</sup> to 1.65 g/cm<sup>3</sup> and  $d_a$  is reduced from 24 μm to 8.7 μm (Fig. 12). The pore ratio  $e$  and  $d_a$  relationship curves are plotted in logarithmic coordinates (Fig. 13), showing a linear relationship between  $e$  and  $d_a$ . The relationship between the  $e$  and the  $d_a$  is given by:

$$\lg e = a \lg d_a + b \tag{9}$$

where  $a$  and  $b$  are parameters of soil properties.

This study takes  $a$  and  $b$  as 0.262 and  $-0.379$ , respectively. Phadnis and Santamarina (2011) also found the same law and concluded that  $e$  and  $d_a$  have a theoretically linear relationship. Comparing

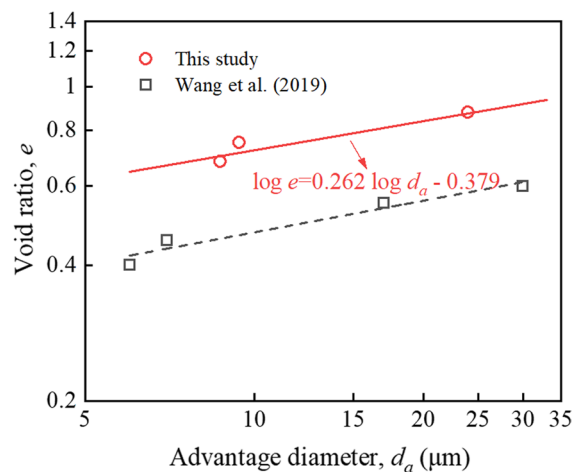


**Fig. 13** Relationship curve between advantage pore size and void ratio

the results of Wang et al. (2019) (Fig. 13), it can be seen that the slope of the linear relationship between  $e$  and  $d_a$  is the same, except for the intercept, which may vary from one soil type to another.

Water flow occurs within the pores in the soil; hence the soil’s permeability is related to its pore size distribution (Greenland et al. 1977; Pagliai et al. 2004). In this paper, the pores are divided based on their size into micropores ( $d < 2 \mu\text{m}$ ), small

pores ( $2 < d < 8 \mu\text{m}$ ), mesopores ( $8 < d < 32 \mu\text{m}$ ), and macropores ( $d > 32 \mu\text{m}$ ) (Lei 1988).

Compared to the  $1.45 \text{ g/cm}^3$  specimen, the  $1.55 \text{ g/cm}^3$  specimen shows a significant decrease in the macropores volume and a slight decrease in the mesopores volume. In contrast, the micropores volume and small pores are unaffected (Fig. 14). When the dry density increases to  $1.65 \text{ g/cm}^3$ , the large pore volume decreases, and the mesopore volume reduces significantly. It is noteworthy that the small pore volume has increased, indicating that the compression of macropores and mesopores produces small pores. On the other hand, the microporous volume reduction is not evident during the whole process. The loess's structural strength mainly comes from the strength and number of particles' contact points (Li et al. 2019a). Therefore, in compression, the large pores are first compressed into smaller ones, and then the object of influence is transformed into a tiny pore size step by step (Oualmakran et al. 2016). The compression of pores is not strictly in the order of pore diameter from large to small. Because the location and direction of each contact point in the loess are different, compressing pores with the same diameter is not the same; thus, the mesopores compression does not start only when the macropores disappear completely. For example, compared to the specimen with a  $\rho_d$  of  $1.45 \text{ g/cm}^3$ , the mesopores volume in the specimen with a  $\rho_d$  of  $1.55 \text{ g/cm}^3$  has started to decrease, but the macropores have not entirely disappeared. The micropores are mainly within the aggregates, and the micropores are the same for different dry densities. This finding is similar to that reported by Zhang et al. (2019a) and Burton et al. (2014).

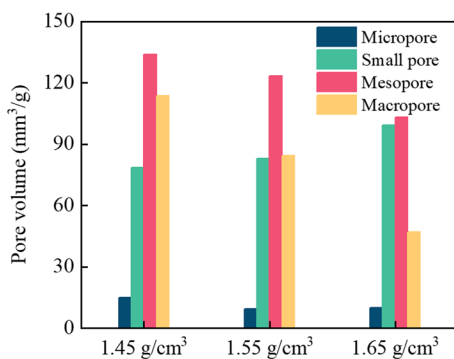


**Fig. 14** Histogram of different types of pore volumes

## 5 Discussions

### 5.1 Response of PSD curve to microstructure

The PSD curve of the  $1.45 \text{ g/cm}^3$  dry density sample shows a double peak, but the difference between the two peaks is enormous, with the prominent peak being seven times the secondary one. The PSD curves of the  $1.55$  and  $1.65 \text{ g/cm}^3$  dry density specimens exhibit a single peak, as shown in Fig. 12. Although the overall change in the micropore volume is not significant (Fig. 14), it is evident from the pore size distribution curve that the micropores are compressed. However, the current study's findings do not support previous research. The traditional understanding of loess pores mainly consists of interaggregate and intra-aggregate pores; hence, the pore size distribution curve should be bimodal (Shao et al. 2018; Li et al. 2020a). Moreover, the loess aggregates exhibit significant stiffness and are affected by the forces generated in static compaction (Barden and Sides Geoffrey 1970). Thus, different specimens have the same micropores (Birle et al. 2008).

The prepared sample water content influences the pore size distribution curve of loess. At lower water contents, capillary action tends to link loess particles and clay grains together and form flocculated structures during sample preparation (Seed and Chan 1959). This indicates that more aggregates are produced when the samples are prepared with low water contents (Delage et al. 1996; Watabe et al. 2000; Monroy et al. 2010). Therefore, the PSD curves of the specimens prepared at low water content exhibit a double peak. When the water reaches the optimum water content, the water pushes the loess units apart in the sample preparation, preventing the formation of aggregates (Fig. 11) (Oualmakran et al. 2016). The distinction between micro- and macro-pores is not apparent, thus showing a single peak (Delage et al. 1996). Therefore, when compressed at optimum water content, a single-peaked pore size distribution curve usually appears and no longer combines micropores and macropores (Delage et al. 1996). When the soil's optimal moisture content is reached, the capillary phenomenon decreases, and the compressibility increases. During compression, the inter-agglomerate pores change, and some large-diameter particles aggregate (Birle et al. 2008). Therefore, the PSD curves at

the micro-pores show signs of compression when the dry density increases (Fig. 12).

## 5.2 Effect of microstructure on water infiltration

Accumulated water infiltration is essentially the process of expelling air from the soil. The low  $w$  of the soil column at the beginning of infiltration resulted in high matric suction (Fig. 8). Therefore, the infiltration rate is faster at the beginning of infiltration. According to the principle of suction equilibrium, water preferentially occupies pores with smaller pore sizes. The micropore volumes of soil columns with different dry densities are the same (Figs. 12 and 14); hence the dry density has no influence on the infiltration and wetting front advance rates of soil columns at the beginning of infiltration. The upper pores of the soil column are the first to be filled with water at the beginning of infiltration, which leads to constant compression of the gas in the pores as the wetting front advances (Touma and Vauclin 1986; Weir and Kissling 1992). The air pressure gradually increases, which means that the wetting front advance and infiltration rates decrease (Figs. 6 and 7). The findings of this section support those of previous studies (Culligan et al. 2000; Essig et al. 2009). As the dry density increases, the macropores within the soil decrease (Fig. 14), and the connectivity between the pores decreases (Fig. 11). The air is expelled more slowly in the soil column with higher dry density and more significant air pressure. Therefore, the decreased degree of the wetting front advance and infiltration rates in the soil column increases with the rise in dry density. When water seeps out at the soil column bottom, the column is close to saturation, and the dry density has a negative effect on the infiltration rate. Consequently, the steady-state infiltration rate is negatively correlated with the dry density (Cho 2016; Sun et al. 2016).

To observe the effect of the PSD curve on the unsaturated permeability more visually, the PSD curve and the unsaturated permeability are plotted with the same coordinate system (Fig. 15). It is noteworthy that the pore diameter is converted to matric suction using the Young–Laplace equation:

$$\psi = \frac{4T_s \cos \alpha}{d} \quad (10)$$

where  $\psi$  is the matric suction (kPa),  $T_s$  is the surface tension at the air–water contact surface (mN/m),  $\alpha$  is

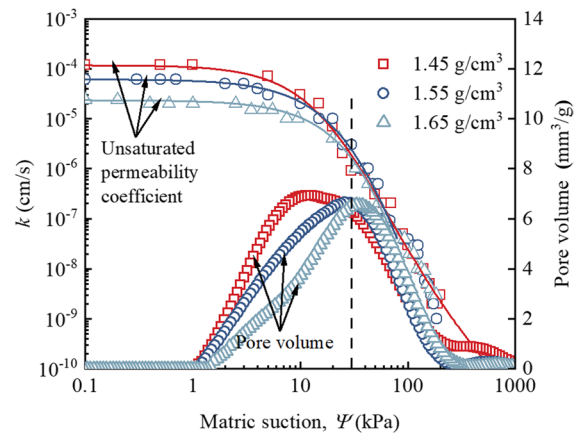


**Fig. 15** Correspondence between unsaturated permeability and PSD curve

the contact angle between the soil and water ( $^\circ$ ), and  $d$  is the pore diameter ( $\mu\text{m}$ ).

Upon seepage initiation, the  $\psi$  gradually decreases, and the maximum diameter of the saturated pore gradually increases. Unsaturated seepage occurs in these saturated pores, so the PSD curve and the unsaturated permeability correspond well. When the  $\psi$  is greater than 30 kPa, the PSD curves of various dry densities overlap, resulting in the same unsaturated permeability. This means that the dry density under high matric suction conditions does not affect the unsaturated permeability of the specimen (Xu et al. 2004). The PSD curve and the permeability no longer overlap when the  $\psi$  is less than 30 kPa. The pore volume decreases with increasing  $\rho_d$  at the same matric suction. The rise in pore volume increases the number of percolation channels and the connectivity between channels. Therefore, the permeability decreases at this stage with increasing dry density (Xu et al. 2004). The permeability remains unchanged when the  $\psi$  is less than 1 kPa. When the  $\psi$  is less than 1 kPa, the pore volume of different dry densities is close to zero, which has almost no effect on the permeability.

## 5.3 Unsaturated permeability model

Darcy's theorem applies to unsaturated soil in a steady flow state (Tian et al. 2020). By Darcy's theorem:

$$k = \frac{Q}{A_i} \tag{11}$$

where  $k$  is the permeability (cm/s),  $Q$  is the sample volume flow rate (cm<sup>3</sup>/s).

Because the soil is composed of massively interconnected pores, seepage occurs (Fig. 11). The pores are divided into  $n$  different sizes (Fig. 16). It is hypothesized that water fills the first  $m$  classes of pores in the soil. Therefore, the pore flow  $Q$  of the sample can be represented as the total of the pore volume flows in the grades up to  $m$  ( $m \leq n$ ):

$$Q = \sum_i^m q_i \tag{12}$$

where  $q_i$  is the volume flow of the  $i$ -th grade pore (cm<sup>3</sup>/s).

According to Hagen Poiseuille, the volume flow  $q_i$  in the pores of grade  $i$  can be expressed as:

$$q_i = \frac{\pi r_i^4 \Delta p}{8 \eta l} N \tag{13}$$

where  $r_i$  is the pore radius ( $\mu\text{m}$ ),  $\Delta p$  is the pressure difference between the two ends of the pore (Pa),  $\eta$  is the viscosity,  $l$  is the pore length (cm), and  $N$  is the number of pores.

Assuming that the ratio of  $l$  to  $L$  is  $P_i$ , the pore length can be expressed as  $LP_i$ . Based on the fractal model theory of pore volume distribution, the

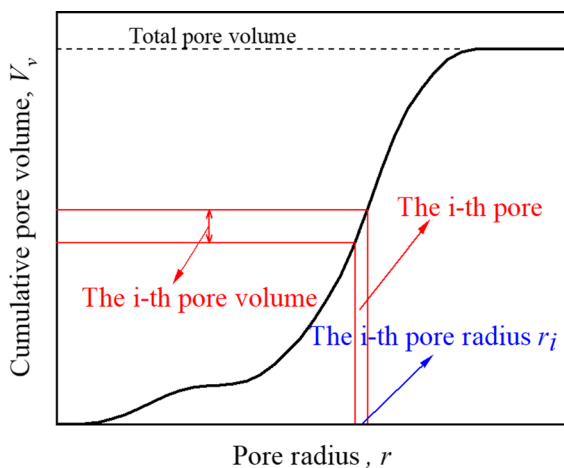


**Fig. 16** Diagram of aperture classification

relationship between pore radius and the corresponding number ( $N$ ) is (Pfeifer and Avnir 1983):

$$N = Cr^{-D} \tag{14}$$

where  $C$  is a constant value,  $D$  is the fractal dimension of pore distribution.

Therefore, Eq. (11) can be expressed as:

$$k = \frac{\sum_{i=1}^m \frac{\pi r_i^4 \Delta p}{8 \eta L p_i} N}{A_i} \tag{15}$$

Since the cross-sectional area of pore in the  $j$ -th grade is defined as  $A_i = \pi r_i^2$  water head loss is defined as  $\Delta h = \Delta p / \rho g$ , and the hydraulic gradient is defined as  $i = \Delta h / L$ , Eq. (15) can be expressed as:

$$k = \frac{\rho g}{8 \eta A} \sum_{i=1}^m \frac{r_i^2 A_i}{p_i} N \tag{16}$$

The volume of pores in the  $i$ th is  $\Delta V_v$ , hence,  $A_i N = \Delta V_v / L p_i$ . For the ideal hypothetical model,  $p_i$  is taken as a constant. Therefore, Eq. (16) can be expressed as:

$$k = \frac{K_c}{V} \sum_{i=1}^m r_i^2 \Delta V_v \tag{17}$$

where  $V$  is the sample volume (cm<sup>3</sup>), and  $K_c = \rho g / (8 \eta p_i^2)$  and for the same soil  $K_c$  is a constant.

From Eq. (14), it can be observed that the pore volume with a pore radius less than  $r$  can be expressed as follows:

$$V_{vr} = \int_0^r \left( \frac{4 \pi r^3}{3} \right) dN = Br^{3-D} \tag{18}$$

where  $B = 4 \pi C D (D-3) / 3$ .

Therefore, Eq. (17) can be expressed in integral form as given below:

$$k = \frac{K_c}{V} \int_0^{V_{vr}} \left( \frac{V}{B} \right)^{\frac{2}{3-D}} dV = \frac{(3-D) K_c}{(5-D) V} \left( \frac{1}{B} \right)^{\frac{2}{3-D}} V_{vr}^{\frac{5-D}{3-D}} \tag{19}$$

The relative permeability ( $k_r$ ) is proportional to the pore volume fraction used for fluid flow, which can be expressed in terms of  $w$  or degree of saturation ( $S_r$ ) (Leij and Wu 1999). When the pores in the soil are filled with liquid ( $V_{vr} = V_v$ ), the permeability

is taken as the saturated permeability  $k_s$ . Therefore, the  $k_r$  can be expressed as:

$$k_r = \frac{k}{k_s} = (S_r)^{\frac{5-D}{3-D}} \quad (20)$$

The only unknown parameters in Eq. (20) are the  $k_s$  and the fractal dimension  $D$ . Among them, the saturated permeability can be obtained through a simple permeability test, so acquiring the fractal dimension is particularly important. Taking the logarithm of the left and right ends in Eq. (18) results in the following equation:

$$\lg V_v = (3 - D) \lg d + \lg \frac{B}{2^{3-D}} \quad (21)$$

It can be seen from Eq. (21) that if the pore volume and pore diameter are the logarithms with base 10, and the slope of the scatter plot is  $k$ , then  $D = 3 - k$ ; therefore, the fractal dimension can be expressed using the formula given as follows (Yu and Li 2001):

$$D = 3 - \frac{\lg V_v}{\lg d_{\max} - \lg d_{\min}} \quad (22)$$

where  $d_{\max}$  and  $d_{\min}$  are the maximum and minimum pore diameters ( $\mu\text{m}$ ), respectively.

Equation (22) considers all pores and applies them to coarse-grained soils. The moisture penetration in loess is mainly in the form of capillary wetting fronts advancing, and capillary water is mainly present in pores with diameters of 2  $\mu\text{m}$  to 500  $\mu\text{m}$  (Wang et al. 2020). The micro-pores are mainly bound to water within them. Therefore, the micro-pore volume ( $V_m$ ) should be neglected when calculating the fractal dimension. Since  $d_{\min} = 2 \mu\text{m}$ , Eq. (22) can be improved as

$$D = 3 - \frac{\lg V_v - \lg V_m}{\lg d_{\max} - \lg 2} \quad (23)$$

where  $V_v$  is a function of the pore ratio that can be expressed as  $e/G_s$ .

Previous studies found that the PSD curve conforms to a normal distribution in semi-logarithmic coordinates and a normal distribution during deformation (Li et al. 2020b). The relationship between the  $d_a$  and the  $d_{\max}$  can be obtained from the normal distribution characteristic ( $\lg d_{\max} = 2 \lg d_a$ ). Based on

the relationship between  $e$  and  $d_{\max}$  (Eq. (9)), the relationship between  $e$  and  $d_{\max}$  can be obtained as follows:

$$\lg d_{\max} = 2 \frac{\lg e - b}{a} \quad (24)$$

Hence, the fractal dimension expression is:

$$D = 3 - \frac{a \lg(e/G_s V_m)}{2 \lg e - 2b - a \lg 2} \quad (25)$$

where parameters  $a$  and  $b$  were previously found,  $V_m$  is considered a fixed parameter (Fig. 14) (Tao et al. 2021), with the value taken as 11.49  $\text{mm}^3/\text{g}$  based on the average of the test results.

The model proposed in this study (Eq. (20) and Eq. (25)) for predicting the unsaturated permeability of loess requires only the void ratio and saturation permeability, which are parameters that can be typically obtained through simple geotechnical tests.

#### 5.4 Model validation

In order to verify the model's accuracy, the unsaturated permeability of the three specimens was predicted as follows:

1. The void ratio ( $e$ ) of the specimen was calculated based on the dry density.
2. The void ratio is substituted into Eq. (24) to find the maximum pore size ( $d_{\max}$ ), where the parameters  $a$  and  $b$  are obtained from Eq. (9).
3. The pore volume ( $V_v$ ) is obtained using the pore ratio, as  $V_v = e/G_s$ .
4. The fractal dimension  $D$  is obtained by substituting  $V_v$ ,  $V_m$  and  $d_{\max}$  into Eq. (23), where  $V_m$  is a constant value for different specimens,  $V_m = 11.49 \text{ mm}^3/\text{g}$ .
5. The unsaturated permeability can be obtained by substituting the fractal dimension and saturated permeability into Eq. (20).

The values of the parameters obtained during the calculations are shown in Table 4.

Figure 17 shows the predicted curve and the measured data, which are in agreement with each other. It indicates that the method provided in this study to predict the unsaturated permeability is feasible.

**Table 4** Predicted parameters of unsaturated permeability

$\rho_d$ (g/cm <sup>3</sup> )	$e$	$V_v$ (mm <sup>3</sup> /g)	$V_m$ (mm <sup>3</sup> /g)	$\lg d_{\max}$ (μm)	$D$	$k_s$ (cm/s)
1.45	0.88	322	11.49	2.77	2.45	1.18E-4
1.55	0.75	275	11.49	2.24	2.31	6.14E-5
1.65	0.64	249	11.49	1.72	2.03	2.35E-5

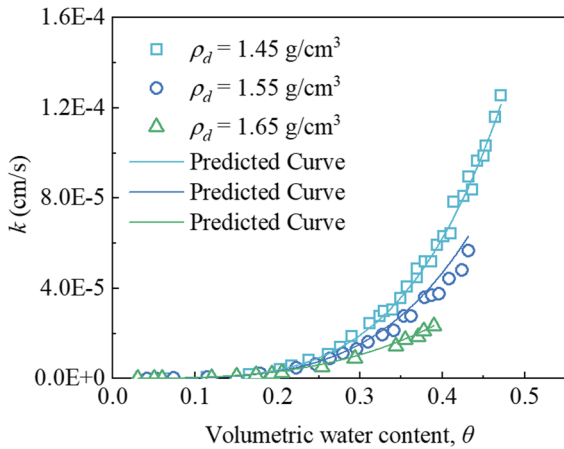


**Fig. 17** Comparison of measured unsaturated permeability and predicted curve

Based on the prediction results, technical guidance can be provided for the early prevention and control of geological hazards such as landslides and foundation instability.

### 6 Conclusions

This study investigates the infiltration characteristics of compacted loess by conducting one-dimensional vertical infiltration tests on soil columns with different dry densities. In addition, it performs SEM and NMR techniques to study the microstructure of soil columns and reveal the mechanism of unsaturated seepage in compacted loess. The main findings of this study are as follows.

1. The infiltration rate and a wetting front advance rate of soil columns with different dry densities decrease with increasing the infiltration time. The initial infiltration and wetting front advancement rate are mainly controlled by the micropore volume and are not affected by the dry density. Once

- the soil column surface layer is saturated, advancing the wetting front generates air pressure and rapidly decreases the advancing rate of the wetting front and the infiltration rate. The pore connectivity controls the wetting front advance rate.
2. The sensor response reflects the advancing wetting front. The response time difference between two adjacent sensors increases with the rise in the burial depth. Besides, the sensor’s response time at the same position increases with the increase in dry density, whereas the wetting front advance rate decrease with the increase in dry density.
  3. The unsaturated permeability increases with the decrease in matric suction. The pore size distribution curves of different dry density specimens are the same when the matric suction is greater than 30 kPa, which is reflected in the fact that the unsaturated permeability in the infiltration curve is not affected by the dry density. The unsaturated permeability decreases with the increase in dry density when the matric suction is less than 30 kPa.
  4. A simple yet efficient unsaturated permeability prediction model based on the void ratio and saturation permeability is proposed in this study. The results show that this model agrees well with the experimental results, indicating that the developed model has satisfactory accuracy.

**Acknowledgements** This study was financially supported by the National Nature Science Foundation of China (Grant no. 41931285) and the key research and development program of Shaanxi Province (Grant no. 2020SF-436; 2019ZDLSF05-07). We would like to thank MogoEdit (<https://www.mogoeedit.com>) for its English editing during the preparation of this manuscript.

**Author contributions** All authors contributed to the study conception and design. HW conducted the experimental study and drafted the manuscript. WN contributed to data curation, funding acquisition, and revision of manuscript. Both authors read and approved the final manuscript.

**Data availability** Data generated or analyzed during this study are available from the corresponding author upon reasonable request.

## Declarations

**Competing interests** The authors declare that they have no known competing financial interests or personal relationships that could have appeared to influence the work reported in this paper.

**Open Access** This article is licensed under a Creative Commons Attribution 4.0 International License, which permits use, sharing, adaptation, distribution and reproduction in any medium or format, as long as you give appropriate credit to the original author(s) and the source, provide a link to the Creative Commons licence, and indicate if changes were made. The images or other third party material in this article are included in the article's Creative Commons licence, unless indicated otherwise in a credit line to the material. If material is not included in the article's Creative Commons licence and your intended use is not permitted by statutory regulation or exceeds the permitted use, you will need to obtain permission directly from the copyright holder. To view a copy of this licence, visit <http://creativecommons.org/licenses/by/4.0/>.

## References:

- Aldaef AA, Rayhani MT (2014) Hydraulic performance of Compacted Clay Liners (CCLs) under combined temperature and leachate exposures. *Waste Manag* 34:2548–2560. <https://doi.org/10.1016/j.wasman.2014.08.007>
- Au SWC (1993) Rainfall and slope failure in Hong Kong. *Eng Geol* 36:141–147. [https://doi.org/10.1016/0013-7952\(93\)90026-9](https://doi.org/10.1016/0013-7952(93)90026-9)
- Barden L, Sides Geoffrey R (1970) Engineering behavior and structure of compacted clay. *J Soil Mech Found Div* 96:1171–1200. <https://doi.org/10.1061/JSFEAQ.0001434>
- Bevington J, Piragnolo D, Teatini P, Vellidis G, Morari F (2016) On the spatial variability of soil hydraulic properties in a Holocene coastal farmland. *Geoderma* 262:294–305. <https://doi.org/10.1016/j.geoderma.2015.08.025>
- Birle E, Heyer D, Vogt N (2008) Influence of the initial water content and dry density on the soil–water retention curve and the shrinkage behavior of a compacted clay. *Acta Geotech* 3:191–200. <https://doi.org/10.1007/s11440-008-0059-y>
- Burton GJ, Sheng D, Campbell C (2014) Bimodal pore size distribution of a high-plasticity compacted clay. *Géotech Lett* 4:88–93. <https://doi.org/10.1680/geolett.14.00003>
- Cai G, Zhou A, Sheng D (2014) Permeability function for unsaturated soils with different initial densities. *Can Geotech J* 51:1456–1467. <https://doi.org/10.1139/cgj-2013-0410>
- Chen H, Lee CF, Law KT (2004) Causative Mechanisms of Rainfall-Induced Fill Slope Failures. *J Geotech Geoenviron Eng* 130:593–602. [https://doi.org/10.1061/\(ASCE\)1090-0241\(2004\)130:6\(593\)](https://doi.org/10.1061/(ASCE)1090-0241(2004)130:6(593))
- Cho SE (2016) Stability analysis of unsaturated soil slopes considering water-air flow caused by rainfall infiltration. *Eng Geol* 211:184–197. <https://doi.org/10.1016/j.enggeo.2016.07.008>
- Culligan PJ, Barry DA, Parlange JY, Steenhuis TS, Haverkamp R (2000) Infiltration with controlled air escape. *Water Resour Res* 36:781–785. <https://doi.org/10.1029/1999WR900351>
- Damiano E, Greco R, Guida A, Olivares L, Picarelli L (2017) Investigation on rainwater infiltration into layered shallow covers in pyroclastic soils and its effect on slope stability. *Eng Geol* 220:208–218. <https://doi.org/10.1016/j.enggeo.2017.02.006>
- Delage P, Audiguier M, Cui Y-J, Howat MD (1996) Microstructure of a compacted silt. *Can Geotech J* 33:150–158. <https://doi.org/10.1139/t96-030>
- Essig ET, Corradini C, Morbidelli R, Govindaraju RS (2009) Infiltration and deep flow over sloping surfaces: Comparison of numerical and experimental results. *J Hydrol* 374:30–42. <https://doi.org/10.1016/j.jhydrol.2009.05.017>
- Fredlund DG, Xing A, Huang S (1994) Predicting the permeability function for unsaturated soils using the soil-water characteristic curve. *Can Geotech J* 31:533–546. <https://doi.org/10.1139/t94-062>
- Galeandro A, Doglioni A, Simeone V, Šimunek J (2014) Analysis of infiltration processes into fractured and swelling soils as triggering factors of landslides. *Environ Earth Sci* 71:2911–2923. <https://doi.org/10.1007/s12665-013-2666-7>
- Gao H, Shao M (2015) Effects of temperature changes on soil hydraulic properties. *Soil Tillage Res* 153:145–154. <https://doi.org/10.1016/j.still.2015.05.003>
- Gao Y, Qian H, Li X, Chen J, Jia H (2018) Effects of lime treatment on the hydraulic conductivity and microstructure of loess. *Environ Earth Sci* 77:529. <https://doi.org/10.1007/s12665-018-7715-9>
- Gao Y, Li Z, Sun DA, Yu H (2021) A simple method for predicting the hydraulic properties of unsaturated soils with different void ratios. *Soil Tillage Res* 209:104913. <https://doi.org/10.1016/j.still.2020.104913>
- Greenland DJ, Pereira HC, Cooke GW, Pirie NW, Bell GDH (1977) Soil damage by intensive arable cultivation: temporary or permanent? *Philos Trans R Soc Lond B Biol Sci* 281:193–208. <https://doi.org/10.1098/rstb.1977.0133>
- Hou K, Qian H, Zhang Q, Lin T, Chen Y, Zhang Y, Qu W (2020) Influence of Quaternary paleoclimate change on the permeability of the loess–paleosol sequence in the Loess Plateau, northern China. *Earth Surf Proc Land* 45:862–876. <https://doi.org/10.1002/esp.4779>
- Jing J, Hou J, Sun W, Chen G, Ma Y, Ji G (2022) Study on influencing factors of unsaturated loess slope stability under dry-wet cycle conditions. *J Hydrol* 612:128187. <https://doi.org/10.1016/j.jhydrol.2022.128187>
- Jones DD, Rowe RK (2016) BTEX migration through various geomembranes and vapor barriers. *J Geotech Geoenviron Eng* 142:04016044. [https://doi.org/10.1061/\(ASCE\)GT.1943-5606.0001502](https://doi.org/10.1061/(ASCE)GT.1943-5606.0001502)
- Kassim A, Gofar N, Lee LM, Rahardjo H (2012) Modeling of suction distributions in an unsaturated heterogeneous



- residual soil slope. *Eng Geol* 131–132:70–82. <https://doi.org/10.1016/j.enggeo.2012.02.005>
- Kong L, Sayem HM, Tian H (2017) Influence of drying–wetting cycles on soil–water characteristic curve of undisturbed granite residual soils and microstructure mechanism by nuclear magnetic resonance (NMR) spin–spin relaxation time (T2) relaxometry. *Can Geotech J* 55:208–216. <https://doi.org/10.1139/cgj-2016-0614>
- Lebeau M, Konrad J-M (2010) A new capillary and thin film flow model for predicting the hydraulic conductivity of unsaturated porous media. *Water Resour Res*. <https://doi.org/10.1029/2010WR009092>
- Lei X (1988) The types of loess pores in China and their relationship with collapsibility; Les types de loess poreux en Chine et leur relation avec les affaissements. *Sci Sin Ser B Chem Biol Agric Med Earth Sci* 31:1398–1410
- Leij F, Wu L (1999) Characterization and measurement of the hydraulic properties of unsaturated porous media. University of California, Riverside
- Li P, Qian H, Wu J (2018) Conjunctive use of groundwater and surface water to reduce soil salinization in the Yinchuan Plain, North-West China. *Int J Water Resour Dev* 34:337–353. <https://doi.org/10.1080/07900627.2018.1443059>
- Li P, Xie W, Pak RYS, Vanapalli SK (2019a) Microstructural evolution of loess soils from the Loess Plateau of China. *CATENA* 173:276–288. <https://doi.org/10.1016/j.catena.2018.10.006>
- Li X-A, Li L, Song Y, Hong B, Wang L, Sun J (2019b) Characterization of the mechanisms underlying loess collapsibility for land-creation project in Shaanxi Province, China—a study from a micro perspective. *Eng Geol* 249:77–88. <https://doi.org/10.1016/j.enggeo.2018.12.024>
- Li L, Li X-A, Wang L, Hong B, Shi J, Sun J (2020a) The effects of soil shrinkage during centrifuge tests on SWCC and soil microstructure measurements. *Bull Eng Geol Env* 79:3879–3895. <https://doi.org/10.1007/s10064-020-01786-y>
- Li P, Shao S, Vanapalli SK (2020b) Characterizing and modeling the pore-size distribution evolution of a compacted loess during consolidation and shearing. *J Soils Sediments* 20:2855–2867. <https://doi.org/10.1007/s11368-020-02621-3>
- Liu Z, Dugan B, Masiello CA, Barnes RT, Gallagher ME, Gonnermann H (2016) Impacts of biochar concentration and particle size on hydraulic conductivity and DOC leaching of biochar–sand mixtures. *J Hydrol* 533:461–472. <https://doi.org/10.1016/j.jhydrol.2015.12.007>
- Ma F, Yang J, Bai X (2017) Water sensitivity and microstructure of compacted loess. *Transp Geotech* 11:41–56. <https://doi.org/10.1016/j.trgeo.2017.03.003>
- Monroy R, Zdravkovic L, Ridley A (2010) Evolution of microstructure in compacted London Clay during wetting and loading. *Géotechnique* 60:105–119. <https://doi.org/10.1680/geot.8.P.125>
- Mualem Y (1976) A new model for predicting the hydraulic conductivity of unsaturated porous media. *Water Resour Res* 12:513–522. <https://doi.org/10.1029/WR012i003p00513>
- Oualmakran M, Mercatoris BCN, François B (2016) Pore-size distribution of a compacted silty soil after compaction, saturation, and loading. *Can Geotech J* 53:1902–1909. <https://doi.org/10.1139/cgj-2016-0184>
- Pagliai M, Vignozzi N, Pellegrini S (2004) Soil structure and the effect of management practices. *Soil Tillage Res* 79:131–143. <https://doi.org/10.1016/j.still.2004.07.002>
- Peng J, Wang S, Wang Q, Zhuang J, Huang W, Zhu X, Leng Y, Ma P (2019) Distribution and genetic types of loess landslides in China. *J Asian Earth Sci* 170:329–350. <https://doi.org/10.1016/j.jseas.2018.11.015>
- Pfeifer P, Avnir D (1983) Chemistry in noninteger dimensions between two and three. I. Fractal theory of heterogeneous surfaces. *J Chem Phys* 79:3558–3565. <https://doi.org/10.1063/1.446210>
- Phadnis HS, Santamarina JC (2011) Bacteria in sediments: pore size effects. *Geotech Lett* 1:91–93. <https://doi.org/10.1680/geolett.11.00008>
- Seed HB, Chan CK (1959) Structure and strength characteristics of compacted clays. *J Soil Mech Found Div* 85:87–128. <https://doi.org/10.1061/JSFEAQ.0000229>
- Shackelford CD, Benson CH, Katsumi T, Edil TB, Lin L (2000) Evaluating the hydraulic conductivity of GCLs permeated with non-standard liquids. *Geotext Geomembr* 18:133–161. [https://doi.org/10.1016/S0266-1144\(99\)00024-2](https://doi.org/10.1016/S0266-1144(99)00024-2)
- Shao X, Zhang H, Tan Y (2018) Collapse behavior and microstructural alteration of remolded loess under graded wetting tests. *Eng Geol* 233:11–22. <https://doi.org/10.1016/j.enggeo.2017.11.025>
- Sun D-M, Li X-M, Feng P, Zang Y-G (2016) Stability analysis of unsaturated soil slope during rainfall infiltration using coupled liquid–gas–solid three-phase model. *Water Sci Eng* 9:183–194. <https://doi.org/10.1016/j.wse.2016.06.008>
- Tao G, Wu Z, Li W, Li Y, Dong H (2021) Simplified relation model of soil saturation permeability and air-entry value and its application. *Fractal Fract* 5:180. <https://doi.org/10.3390/fractalfract5040180>
- Tian K, Yang A, Nie K, Zhang H, Xu J, Wang X (2020) Experimental study of steady seepage in unsaturated loess soil. *Acta Geotech* 15:2681–2689. <https://doi.org/10.1007/s11440-020-00948-2>
- Touma J, Vauclin M (1986) Experimental and numerical analysis of two-phase infiltration in a partially saturated soil. *Transp Porous Media* 1:27–55. <https://doi.org/10.1007/BF01036524>
- Wagner B, Tarnawski VR, Hennings V, Müller U, Wessolek G, Plagge R (2001) Evaluation of pedo-transfer functions for unsaturated soil hydraulic conductivity using an independent data set. *Geoderma* 102:275–297. [https://doi.org/10.1016/S0016-7061\(01\)00037-4](https://doi.org/10.1016/S0016-7061(01)00037-4)
- Wang W, Wang Y, Sun Q, Zhang M, Qiang Y, Liu M (2018) Spatial variation of saturated hydraulic conductivity of a loess slope in the South Jingyang Plateau, China. *Eng Geol* 236:70–78. <https://doi.org/10.1016/j.enggeo.2017.08.002>
- Wang J-D, Li P, Ma Y, Vanapalli SK (2019) Evolution of pore-size distribution of intact loess and remolded loess due to consolidation. *J Soils Sediments* 19:1226–1238. <https://doi.org/10.1007/s11368-018-2136-7>
- Wang J, Zhang D, Chen C, Wang S (2020) Measurement and modelling of stress-dependent water permeability of

- collapsible loess in China. *Eng Geol* 266:105393. <https://doi.org/10.1016/j.enggeo.2019.105393>
- Wang H-M, Ni W-K, Yuan K-Z, Li L, Nie Y-P, Guo Y-X (2021a) Microstructure evolution of loess under multiple collapsibility based on nuclear magnetic resonance and scanning electron microscopy. *J Mt Sci* 18:2612–2625. <https://doi.org/10.1007/s11629-021-6838-8>
- Wang H, Ni W, Li X, Li L, Yuan K, Nie Y (2021b) Predicting the pore size distribution curve based on the evolution mechanism of soil–water characteristic curve. *Environ Earth Sci* 81:23. <https://doi.org/10.1007/s12665-021-10138-2>
- Wang H, Ni W, Liu H, Huang M, Yuan K, Li L, Li X (2021c) Study of the repeated collapsibility of undisturbed loess in Guyuan, China. *Bull Eng Geol Env* 80:6321–6330. <https://doi.org/10.1007/s10064-021-02304-4>
- Watabe Y, Leroueil S, Le Bihan JP (2000) Influence of compaction conditions on pore-size distribution and saturated hydraulic conductivity of a glacial till. *Can Geotech J* 37:1184–1194. <https://doi.org/10.1139/t00-053>
- Wei Y-N, Fan W, Yu B, Deng L-S, Wei T (2020) Characterization and evolution of three-dimensional microstructure of Malan loess. *CATENA* 192:104585. <https://doi.org/10.1016/j.catena.2020.104585>
- Weir GJ, Kissling WM (1992) The influence of airflow on the vertical infiltration of water into soil. *Water Resour Res* 28:2765–2772. <https://doi.org/10.1029/92WR00803>
- Xie W-L, Li P, Zhang M-S, Cheng T-E, Wang Y (2018) Collapse behavior and microstructural evolution of loess soils from the Loess Plateau of China. *J Mt Sci* 15:1642–1657. <https://doi.org/10.1007/s11629-018-5006-2>
- Xu Y-F, Ye C-M, Zhao S-Q, Xia X-H (2004) Effect of compressive stress on hydraulic conductivity of unsaturated soils. *Shanghai Jiaotong Daxue Xuebao* 38:982–986
- Xu P, Zhang Q, Qian H, Hou K (2020) Investigation into microscopic mechanisms of anisotropic saturated permeability of undisturbed Q2 loess. *Environ Earth Sci* 79:412. <https://doi.org/10.1007/s12665-020-09152-7>
- Xu P, Zhang Q, Qian H, Li M, Yang F (2021) An investigation into the relationship between saturated permeability and microstructure of remolded loess: a case study from Chinese Loess Plateau. *Geoderma* 382:114774. <https://doi.org/10.1016/j.geoderma.2020.114774>
- Yu B, Li J (2001) Some fractal characters of porous media. *Fractals* 09:365–372. <https://doi.org/10.1142/s0218348x01000804>
- Yuan K-Z, Ni W-K, Lü X-F, Zhu M (2022) Experimental study on the performance of the modified loess by polypropylene fiber mixed with bentonite and cement. *Bull Eng Geol Environ* 81:302. <https://doi.org/10.1007/s10064-022-02800-1>
- Zand-Parsa S, Sepaskhah AR (2004) Soil hydraulic conductivity function based on specific liquid–vapor interfacial area around the soil particles. *Geoderma* 119:143–157. [https://doi.org/10.1016/S0016-7061\(03\)00258-1](https://doi.org/10.1016/S0016-7061(03)00258-1)
- Zhang W, Sun Y, Chen W, Song Y, Zhang J (2019a) Collapsibility, composition, and microfabric of the coastal zone loess around the Bohai Sea, China. *Eng Geol* 257:105142. <https://doi.org/10.1016/j.enggeo.2019.05.019>
- Zhang X, Lu Y, Li X, Lu Y, Pan W (2019b) Microscopic structure changes of Malan loess after humidification in South Jingyang Plateau, China. *Environ Earth Sci* 78:287. <https://doi.org/10.1007/s12665-019-8290-4>
- Zhuang J, Nakayama K, Yu GR, Miyazaki T (2001) Predicting unsaturated hydraulic conductivity of soil based on some basic soil properties. *Soil Tillage Res* 59:143–154. [https://doi.org/10.1016/S0167-1987\(01\)00160-X](https://doi.org/10.1016/S0167-1987(01)00160-X)

**Publisher's Note** Springer Nature remains neutral with regard to jurisdictional claims in published maps and institutional affiliations.